

Vortices in p -Wave Superfluids of Trapped Fermionic Atom Gases

Yasumasa Tsutsumi* and Kazushige Machida

Department of Physics, Okayama University, Okayama 700-8530

(Received May 29, 2018)

In order to help detecting superfluidity, we theoretically investigate p -wave pairing superfluids in neutral Fermion atom gases confined by a three dimensional (3D) harmonic potential. The Ginzburg-Landau framework, which is generic for p -wave superfluids, is used to describe the order parameter spatial structure, or texture characterized by the l -vector both at rest and under rotation. The l -vector configuration is strongly constrained by the boundary condition due to a trap. It is found that the ground state textures exhibit spontaneous supercurrent at rest both cigar and pancake shape traps. The current direction depends on the trapping shape. Under rotation a pair of half-quantum vortex with half-winding number enters a system and is stabilized for both trap geometries. We give detailed explanation for their 3D structure. The deformations of the condensate shape are seen with increasing the rotation speed, which is tightly connected with the underlying vortex formation where the condensates are depressed in the vortex core.

KEYWORDS: p -wave pairing, superfluids, neutral Fermion atom gases, texture, vortex

1. Introduction

Superfluids with multi-component order parameter (OP) are omnipresent, exemplified by spinor Bose-Einstein condensates (BEC)¹⁻⁴⁾ in cold Bosonic atom gases with ^{23}Na or ^{87}Rb , strongly interacting Fermionic liquid ^3He atoms,⁵⁻⁹⁾ and certain heavy Fermion superconductors, such as UPt_3 ^{10,11)} or color superconductivity in dense quark-gluon plasmas in high energy physics.^{12,13)} This branch of physics is of great interest from a fundamental physics view point as it is expected to exhibit rich topological defect structures or vortices and allow investigation of a new phase of matter. Those vortices that can accommodate the Majorana zero mode at the core may be useful in quantum computing.¹⁴⁾ We will show in this paper that half-quantum vortices (HQV) are stabilized, which is a candidate to lead to the Majorana particles in the core.¹⁴⁾ Therefore the present p -wave superfluids in general provide a testing ground to explore rich physics associated with topological defects. Previously we have demonstrated that superfluid $^3\text{He-A}$ phase is another fertile ground to find the Majorana particle.^{15,16)} This is the second example to show HQV as a stable vortex in our study¹⁶⁾ where superfluid $^3\text{He-A}$ phase confined between parallel plates is demonstrated to exhibit HQV.

*E-mail address: tsutsumi@mp.okayama-u.ac.jp

Recently, p -wave resonance superfluidity attracts much attention in Fermionic alkaline atom gases, such as ${}^6\text{Li}$ ^{17–19)} and ${}^{40}\text{K}$,^{20–22)} both experimentally and theoretically.^{23–27)} Experiments into achieving p -wave resonance superfluidity are steadily progressing¹⁹⁾ and hence it is timely and necessary to consider the generic properties of p -wave superfluidity both at rest and under rotation to detect its superfluidity, which is signified by non-trivial topological structures or vortices. In this respect, the interest is in the spatial structure, i.e. texture, of the nine component OPs describing the spin triplet p -wave superfluidity. A p -wave Feshbach resonance occurs at the different magnetic field in each hyperfine spin state of Cooper pair. Since the spin state of superfluidity is fixed by the external magnetic field, the spin degrees of freedom are frozen, and hence only the orbital degrees of freedom are active. The order parameter space consisting of orbital three components is analogous to that of superfluid ${}^3\text{He}$, in particular, the A phase to which spin and orbital state can be separated,^{5–8)} where the OP is described by a tensor

$$A_{\mu i} = d_{\mu} A_i \quad (\mu, i = x, y, z). \quad (1)$$

The d_{μ} and A_i describe the spin and orbital state of a Cooper pair, respectively. Here the OP is characterized only by A_i , described as

$$\Delta(\hat{\mathbf{p}}) = A_x \hat{p}_x + A_y \hat{p}_y + A_z \hat{p}_z. \quad (2)$$

In a sense, a p -wave superfluid is analogous to the “spinless” superfluid ${}^3\text{He}$ -A phase.¹⁵⁾

The dipole-dipole interaction between two alkaline atoms acts to split the relative orbital state for two particles, depending on the projections of the orbital angular momentum, either $m_l = \pm 1$ or $m_l = 0$. This results in breaking of the degeneracy between

$$\hat{p}_{\pm} = \mp \frac{1}{\sqrt{2}} (\hat{p}_x \pm i \hat{p}_y) \quad \text{and} \quad \hat{p}_0 = \hat{p}_z. \quad (3)$$

This splitting was estimated to be large for ${}^{40}\text{K}$ by Cheng and Yip,²³⁾ evidenced by the clear difference in the Feshbach resonance magnetic fields (splitting field = $0.47 \pm 0.08\text{G}$).²¹⁾ For ${}^6\text{Li}$, the splitting may be small, as an experiment conducted in a magnetic field of $H = 158.5(7)\text{G}$ shows no clear resonance splitting.¹⁹⁾

A critical difference between superfluid ${}^3\text{He}$ and a p -wave resonance superfluid of atom gases lies in the boundary conditions. In the superfluid ${}^3\text{He}$ -A phase the l -vector, which is the orbital angular momentum of Cooper pairs, is always perpendicular to a hard wall so that the perpendicular particle motion is suppressed. In other words, the point nodes in the l -vector direction touch the hard wall so as to minimize the condensation energy loss at the boundary.⁶⁾ On the other hand, atom gases are confined by a three dimensional (3D) harmonic trap potential, where the condensation energy density gradually decreases towards the outer region, the l -vector tends to align parallel to the circumference. This orientation is advantageous because the condensation energy is maximally gained by allowing the point

nodes to move out from the system. The trap potential is easily controlled, resulting in various shapes, such as cigar or pancake shapes. As we describe below, the trapping potential can be an important tool to control the 3D texture. Indeed, the 3D trapping structure constrains the possible textures. Our purpose is to investigate a possible 3D textures in a 3D harmonic trap potential and thereby to help identifying p -wave superfluidity.

The organization of this paper is as follows: We employ the Ginzburg-Landau (GL) framework which relies only on global symmetry principle. The GL free energy functional form is introduced and the relevant physical quantities, such as supercurrent and l -vector are given in § 2. We show the phase diagram of the stable states for uniform and infinite system, and explain how to numerically examine realistic confined systems in § 3. Section 4 presents the stable texture in the cigar shape trap, especially, we mention the spontaneous supercurrent at rest and the half-quantum vortex (HQV) under rotation. In § 5, we show the different textures stabilized in the pancake shape. The final § 6 is devoted to a summary and discussion. A short version of the present paper is to be published.²⁸⁾

2. Formulation

Here we employ the GL framework.⁶⁾ This framework is general and flexible enough to allow us to examine a generic topological structure, and applicable to cold Fermionic atom gases with a harmonic trap potential under $k_B T_c \gg \hbar\omega$, where T_c and ω are the transition temperature and the trap frequency, respectively.²⁹⁾ In terms of the tensor $A_{\mu i}$ forming OP of p -wave pairing the most general GL functional density f_{bulk} for the bulk condensation energy up to fourth order is described as

$$f_{\text{bulk}} = -\alpha_i A_{\mu i}^* A_{\mu i} + \beta_1 A_{\mu i}^* A_{\mu i}^* A_{\nu j} A_{\nu j} + \beta_2 A_{\mu i}^* A_{\mu i} A_{\nu j}^* A_{\nu j} + \beta_3 A_{\mu i}^* A_{\nu i}^* A_{\mu j} A_{\nu j} \\ + \beta_4 A_{\mu i}^* A_{\nu i} A_{\nu j}^* A_{\mu j} + \beta_5 A_{\mu i}^* A_{\nu i} A_{\nu j} A_{\mu j}^*, \quad (4)$$

which is invariant under spin and real space rotations in addition to the gauge invariance $U(1) \times SO^{(S)}(3) \times SO^{(L)}(3)$. The fourth order terms are characterized by five independent invariants, $\beta_1 \sim \beta_5$ in general.⁶⁾ Since the spin degrees of freedom are frozen due to applied magnetic field for magnetic Feshbach resonance, only the orbital degrees of freedom A_i in $A_{\mu i} = d_{\mu} A_i$ are active. Namely it reduces to

$$f_{\text{bulk}} = -\alpha_0(1 - t_i) A_i^* A_i + \beta_{24} A_i^* A_i A_j^* A_j + \beta_3 A_i^* A_i^* A_j A_j, \quad (5)$$

where $\beta_{24} = \beta_2 + \beta_4$ and $t_i = T/T_{ci}$ (T_{ci} is the transition temperature for the i -component). As mentioned, the dipole-dipole interaction causes splitting of the transition temperatures into two groups $T_{cx} = T_{cy}$ and T_{cz} . We introduce $\alpha = T_{cx}/T_{cz}$, which indicates the degree of the broken symmetry of the system and characterizes atomic species used.²¹⁾ The pairing state having the orbital projection $m_l = 0$ is favorable over $m_l = \pm 1$, namely $0 < \alpha < 1$ due to the dipole-dipole interaction.²¹⁾ The three components become degenerate for $\alpha \rightarrow 1$. When

$\alpha \rightarrow 0$, the polar state with the OP $\Delta(\hat{\mathbf{p}}) = A_z \hat{p}_z$ tends to be stable.

The gradient energy consisting of the three independent terms⁶⁾ is given by

$$f_{\text{grad}} = K_1(\partial_i^* A_j^*)(\partial_i A_j) + K_2(\partial_i^* A_j^*)(\partial_j A_i) + K_3(\partial_i^* A_i^*)(\partial_j A_j). \quad (6)$$

The centrifugal potential energy due to rotation with $\mathbf{\Omega}$, which is derived in Appendix A, is written as

$$f_{\text{cent}} = -\frac{m^2}{\hbar^2} \Omega^2 \rho^2 (K_1 A_i^* A_i + K_2 |A_\theta|^2 + K_3 |A_\theta|^2), \quad (7)$$

where $\partial_i = \nabla_i - i(m/\hbar)(\mathbf{\Omega} \times \mathbf{r})_i$. For $\mathbf{\Omega} \parallel \hat{\mathbf{z}}$, $\rho^2 = x^2 + y^2$ and $A_\theta = -A_x \sin \theta + A_y \cos \theta$ in the cylindrical coordinates.

The GL parameters α_0 , $\beta_{24} = \beta_2 + \beta_4$, β_3 and $K_1 = K_2 = K_3 = K$ are estimated by taking the weak coupling approximation, assuming the Fermi sphere:⁶⁾

$$\alpha_0 = \frac{N(0)}{3}, \quad \beta_2 = \beta_3 = \beta_4 = \frac{7\zeta(3)N(0)}{120(\pi k_B T_c)^2} \equiv \beta \quad (8)$$

and

$$K = \frac{7\zeta(3)N(0)(\hbar v_F)^2}{240(\pi k_B T_c)^2} \quad (9)$$

where $N(0)$ is the density of states at the Fermi level and v_F is the Fermi velocity. The weak coupling approximation should be a good guide for understanding the generic properties of the p -wave superfluids of atom gases because it has been applied successfully, even to liquid ^3He with strong interacting Fermions and only small additional strong corrections.⁶⁾

It is convenient to discuss (5), (6) and (7) in the following dimensionless units,

$$\frac{A_i}{A^{(0)}} \rightarrow A_i, \quad \frac{r}{\xi_0} \rightarrow r, \quad \frac{\Omega}{\Omega^{(0)}} \rightarrow \Omega \quad (10)$$

with the zero-temperature GL coherence length

$$\xi_0 = \sqrt{\frac{K}{\alpha_0}} = \sqrt{\frac{7\zeta(3)}{80\pi^2} \frac{\hbar v_F}{k_B T_c}}. \quad (11)$$

The units of OP and the angular velocity are

$$A^{(0)} = \sqrt{\frac{\alpha_0}{2\beta}} = \sqrt{\frac{20\pi^2}{7\zeta(3)}} k_B T_c, \quad (12)$$

$$\Omega^{(0)} = \frac{\hbar}{m} \frac{1}{\xi_0^2}. \quad (13)$$

In the dimensionless unit, (5), (6) and (7) are written as

$$f_{\text{bulk}} = - (1 - t_i) A_i^* A_i + A_i^* A_i A_j^* A_j + \frac{1}{2} A_i^* A_i^* A_j A_j, \quad (14)$$

$$f_{\text{grad}} = (\partial_i^* A_j^*)(\partial_i A_j) + (\partial_i^* A_j^*)(\partial_j A_i) + (\partial_i^* A_i^*)(\partial_j A_j), \quad (15)$$

$$f_{\text{cent}} = - \Omega^2 \rho^2 (A_i^* A_i + 2|A_\theta|^2), \quad (16)$$

respectively, where $\partial_i = \nabla_i - i(\mathbf{\Omega} \times \mathbf{r})_i$. From now on we use the dimensionless expressions.

The harmonic trap potential term²⁹⁾ is

$$f_{\text{harmonic}} = \omega_{\perp}^2 (\rho^2 + \lambda^2 z^2) A_i^* A_i, \quad (17)$$

where the dimensionless radial confining potential is ω_{\perp} and the anisotropy of the harmonic trap is expressed as $\lambda \equiv \omega_z/\omega_{\perp}$. The harmonic trap potential term acts to lower the transition temperatures. It is interesting to note that the centrifugal potential leads to the non-trivial form, because the OP label implies the orbital angular momentum, a feature absent in a spinor BEC.³⁰⁾ The extra factor of $2|A_{\theta}|^2$ in the above form of (16) becomes important when evaluating the critical angular velocity Ω_{cr} , above which the superfluid flies apart. That is, $\Omega_{\text{cr}} = \omega_{\perp}/\sqrt{3}$ is greatly reduced from the usual case ($\Omega_{\text{cr}} = \omega_{\perp}$).

The relevant physical quantities are described in terms of the OP $A_i(\mathbf{r})$ as follows. The total free energy:

$$F = \int d^3r (f_{\text{bulk}} + f_{\text{grad}} + f_{\text{cent}} + f_{\text{harmonic}}). \quad (18)$$

The current density:

$$j_i(\mathbf{r}) \equiv 2\text{Im} [A_j^* \nabla_i A_j + A_j^* \nabla_j A_i + A_i^* \nabla_j A_j]. \quad (19)$$

The l -vector:

$$l_i(\mathbf{r}) \equiv -i\epsilon_{ijk} \frac{A_j^* A_k}{|\Delta(\mathbf{r})|^2} \quad (20)$$

with

$$|\Delta(\mathbf{r})|^2 = A_i^* A_i. \quad (21)$$

3. Preriminary Considerations

Before considering a realistic confined system, we first investigate an infinite system at rest. Then the state minimizing the condensation energy (14) is realized. As shown in Appendix B, the phase diagram in Fig. 1 consists of the three phases, A, B, and normal (N) phases. The B phase is described by $\Delta(\hat{\mathbf{p}}) = A_z \hat{p}_z$, i.e. the polar state. The A phase is described by a chiral OP expressed by

$$\Delta(\hat{\mathbf{p}}) = A_z (\hat{p}_z + i\gamma \hat{p}_{\perp}), \quad (22)$$

where ($0 < \gamma \leq 1$) with $\hat{p}_{\perp} = \hat{p}_x \cos \phi + \hat{p}_y \sin \phi$ (ϕ is arbitrary). This phase breaks the time reversal symmetry. The value of γ depends on temperature and anisotropy α ,

$$\gamma = \frac{2 - (3 - \alpha)t_x}{2 + (1 - 3\alpha)t_x}. \quad (23)$$

In the absence of the dipole-dipole interaction ($\alpha = 1$), the value of γ is unity. As the dipole-dipole interaction increases (α decreases), γ decreases. The decrease of γ becomes larger at high temperature. When the value of γ vanishes, the second order transition from the A phase

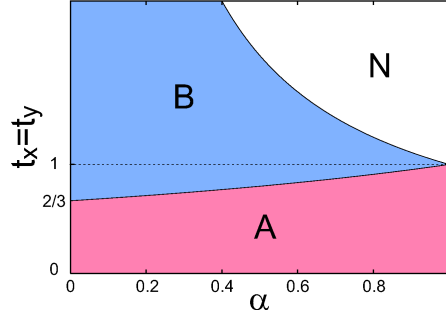


Fig. 1. (Color online) Phase diagram of the p -wave pairing state in an infinite system at rest, showing temperature ($t_x = t_y$) versus anisotropy $\alpha \equiv T_{cx}/T_{cz}$. N: normal state, A: chiral state $A_z(\hat{p}_z + i\gamma\hat{p}_\perp)$ and B: polar state $A_z\hat{p}_z$.

to the B phase takes place. The transition temperature t_c is given by

$$t_c = \frac{2}{3 - \alpha}. \quad (24)$$

The phase diagram corresponds to the case being not so large Feshbach resonance splitting in BCS regime.²⁴⁾ However, it is warned that the determined phase boundary is of qualitative at low temperatures which is beyond the GL framework. In the following we examine the A phase in confined geometries.

In order to obtain stable texture of the condensates in a realistic harmonic potential, we have identified stationary solutions by numerically solving the variational equations: $\delta f(\mathbf{r})/\delta A_i(\mathbf{r}) = 0$ in three dimensions where $f(\mathbf{r})$ is the GL energy density functional, the integrand of (18). We start with various initial configurations, including singular vortex state and non-singular vortex state, and determine the most stable texture by comparing the total GL energy (18).

4. Cigar Shape Trap

We first consider the stable texture for a cigar shape trap with the trap anisotropy $\lambda = 0.2$. We take $80 \times 80 \times 120$ meshes with the cloud sizes for the Thomas-Fermi approximation $R_x = R_y = 10$ and $R_z = 50$. We fix the temperature at $t_x = t_y = 0.4$ and the anisotropy parameter $\alpha = 0.9$.

4.1 Stable texture at rest

The stable l -vector texture at rest is shown in Fig. 2. Figure 2(a) displays the amplitude distribution of the l -vectors. It can be seen that the amplitude $|\mathbf{l}|$ is maximum in the central region, and towards the outer regions $|\mathbf{l}|$ decreases gradually. At the top and bottom ends, the polar state is realized where the l -vector vanishes. Three cross sections are shown in Figs. 2(b)-(d). In Fig. 2(c), which corresponds to the middle cross section, the l -vectors lie in the x - y plane, showing a streamline type pattern in which the l -vectors follow the circumference,

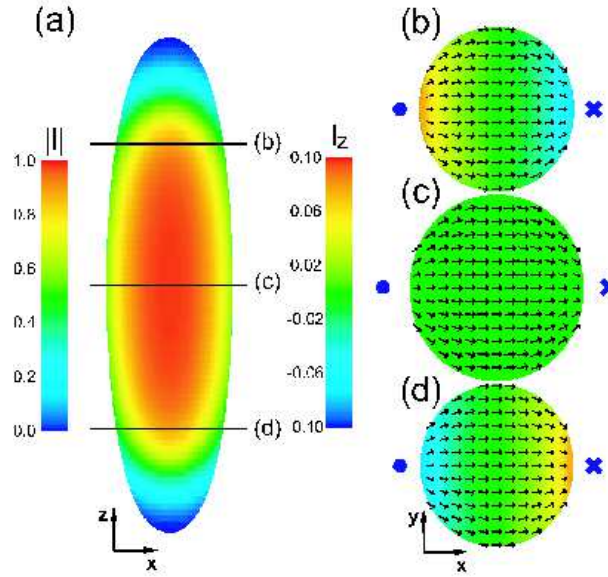


Fig. 2. (Color online) Stable texture at rest for cigar trap $\lambda = 0.2$. (a) Distribution of $|l|$ in the z - x plane. (b)-(d) Three cross sections indicated in (a), showing l_z (color) and l_x and l_y components (arrows), where the dot and cross marks indicate the imaginative source and sink for the l -vector stream lines.

like a fluid streaming along a circular boundary. Outside the condensates, an unseen sink and source of the l -vectors exist, giving two imaginary focal points situated outside. Namely the left dot and right cross marks in Figs. 2(b)-(d) correspond to the source and sink where the l -vectors appear and disappear. This streamline like texture contrasts with the so-called Pan-Am texture in superfluid $^3\text{He-A}$ phase⁶⁾ where the l -vectors tend to point perpendicular to the wall due to the boundary condition. In the upper (Fig. 2(b)) and lower (Fig. 2(d)) cross sections the streamline texture is maintained, but an l_z component appears in addition.

The associated supercurrent structure is depicted in Fig. 3. The j_z component shows a circulation supercurrent along the z axis (see Fig. 3(a)). Since $\Omega = 0$, this circulation supercurrent is spontaneously generated. This non-trivial condensates flow can be explained in supercurrent characteristic of chiral p -wave superfluid:

$$\mathbf{j} = \rho_s \mathbf{v}_s + \mathbf{C}(\nabla \times \mathbf{l}), \quad (25)$$

where ρ_s and \mathbf{C} are diagonal tensor coefficients. The supercurrent has a structure that is similar to that for the total charge-current density of a system in classical electrodynamics. The current in classical electrodynamics is composed of two parts, the actual charge transport and an effective current in proportion to $\nabla \times \mathbf{M}$ due to the magnetization \mathbf{M} generated by the internal motion of the electrons. In chiral p -wave superfluid the Cooper pair may be thought of as representing the atom and \mathbf{l} the magnetic orbital moment \mathbf{M} . Therefore the first term in the supercurrent describes the usual flow of Cooper pairs, while the second one is an “orbital”

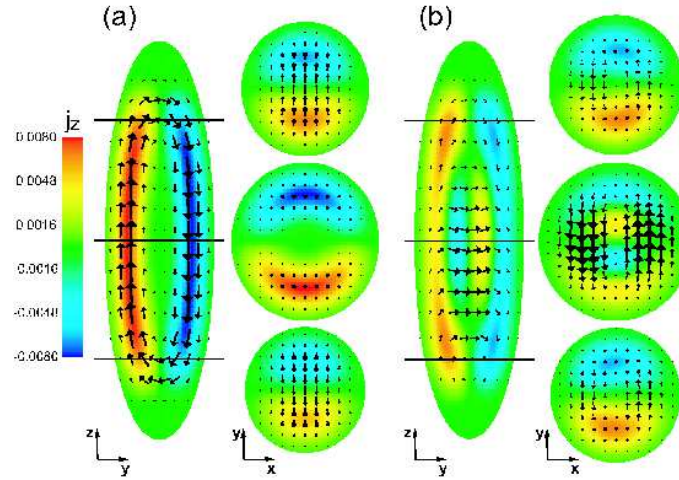


Fig. 3. (Color online) (a) Spontaneous circulating current flows at rest ($\Omega = 0$) in the z - y plane along the z direction. Three cross sections indicated in the left figure, showing j_z (color) and j_x and j_y components (arrows). (b) The current pattern under rotation ($\Omega = 0.3$). It is seen that the in-plane components j_x and j_y increase, producing the in-plane circular current due to rotation.

supercurrent driven by the spatial variation of the l -vector.

In this system, the spontaneous supercurrent is not a usual supercurrent $\rho_s \mathbf{v}_s$ but an “orbital” supercurrent $\mathbf{C}(\nabla \times \mathbf{l})$ with the trap potential. In the middle cross section in Fig. 3(a), the l -vector in-plane bending $(\nabla \times \mathbf{l})_z$ produces a perpendicular current j_z . However, at the upper and lower planes in Fig. 3(a), the supercurrent acquires the j_x and j_y components because of the non-vanishing l_z component. Therefore, the perpendicular current at the center bends such that the condensates are conserved. It is clear from Fig. 3(a) that the supercurrent circulates perpetually along the z direction parallel to the long axis of the trap. This result is non-trivial and a remarkable manifestation in the topological nature of the texture.

In Fig. 3(b) we also display the current patterns under rotation ($\Omega = 0.3\omega_\perp$) for comparison at rest. It is seen that the in-plane components j_x and j_y increase, producing the in-plane circular current due to rotation, in particular in the middle cross section. Thus under rotations, the current consists of the spontaneous one along the z direction and the induced circular current in the plane.

4.2 Half-quantum vortex under rotation

In Fig. 4 where we depict the middle cross sections of the stable solutions for various rotation speeds (also see Fig. 6). It is seen that under rotation, the 3D texture deforms continuously and smoothly. As the rotational speed increases, the l -vectors in the x - y plane pointing in the x direction acquire a negative z component, as seen by the color change from green to blue. This deformation yields in plane circular “orbital” supercurrent as already shown in Fig. 3(b).

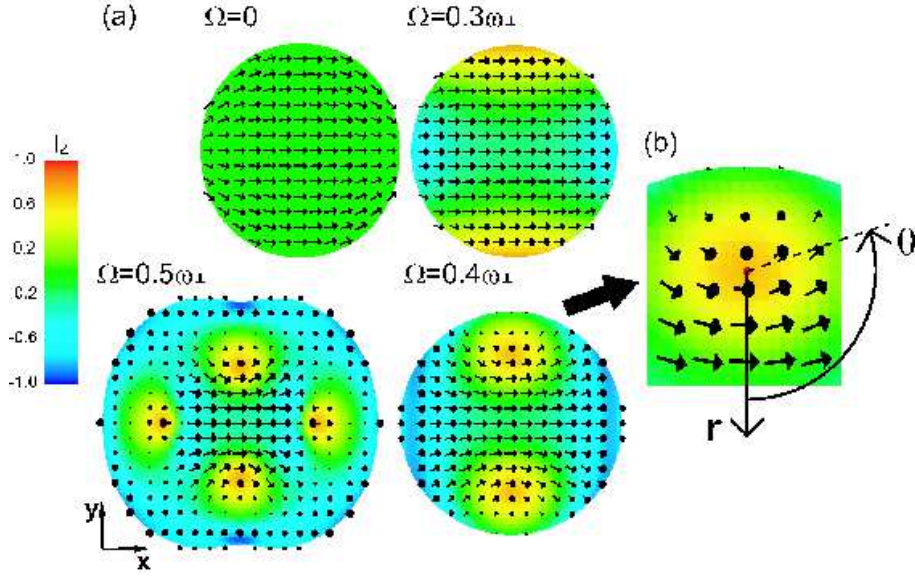


Fig. 4. (Color online) (a) Texture change with rotational speed Ω relative to the in-plane trap frequency ω_{\perp} . Middle cross sections are displayed showing l_z (color) and l_x and l_y components (arrows). As Ω increases, l -vectors acquire a negative z component (seen as a color change). At $\Omega = 0.4\omega_{\perp}$ two plus HQVs enter from the y direction seen as yellow objects. At $\Omega = 0.5\omega_{\perp}$ four plus HQVs and two minus HQVs are present and the condensates expand and deform. (b) The enlarged figure of HQV where the local coordinates (r, θ) are shown.

Above a certain rotational speed ($\Omega = 0.4\omega_{\perp}$), two HQVs enter from the y direction, where the l -vector at the core pointing in the positive z direction, as seen by the yellow objects. The OP far away from the HQV core is described in terms of the local coordinated (r, θ) centered at the core (see Fig. 4(b)) as

$$\Delta(r \gg 1, \theta, \hat{\mathbf{p}}) = \exp[i(\theta/2 + \pi/2)]|A_{xy}|[\sin(\theta/2)\hat{p}_x - \cos(\theta/2)\hat{p}_y] + |A_z|\hat{p}_z, \quad (26)$$

where $|A_{xy}|$ and $|A_z|$ are amplitude of the polar state characterized by the basis functions $\hat{p}_x\hat{p}_y$ (x - y polar state) and by \hat{p}_z (z polar state), respectively. The HQV is formed by only the x - y polar state as is seen from (26). The above state (26) can be written as

$$\Delta(r \gg 1, \theta, \hat{\mathbf{p}}) = \frac{1}{\sqrt{2}}|A_{xy}|(\hat{p}_+ + e^{i\theta}\hat{p}_-) + |A_z|\hat{p}_0. \quad (27)$$

The vortex core of this HQV has the orbital angular momentum with positive z component because \hat{p}_+ is non-vanishing there, so we define it as a plus HQV. Similarly, one can construct a minus HQV with the identical vorticity but the local orbital angular momentum of the negative z component in its core (\hat{p}_-).

The realized OP written as

$$\Delta(\mathbf{r}, \hat{\mathbf{p}}) = A_+(\mathbf{r})\hat{p}_+ + A_-(\mathbf{r})\hat{p}_- + A_0(\mathbf{r})\hat{p}_0, \quad (28)$$

$$A_{\pm} = \mp \frac{1}{\sqrt{2}}(A_x \mp iA_y), A_0 = A_z \quad (29)$$

is shown in Fig. 5(a) where the amplitudes (upper line) and phases (lower line) for each component A_+ , A_- , A_0 are displayed for $\Omega = 0.4\omega_{\perp}$ corresponding to Fig. 4. It is seen that there are two vortices with the winding number 1 in A_- component on the y axis. The depletion of the OP amplitude by the vortices is compensated by the growth of A_+ amplitude. The HQV is embedded in the surrounding OP field. As we walk around one of the HQV core, the p -wave pairing state changes in the following manner: At $\theta = \pi$, the OP is described as $\Delta(\hat{\mathbf{p}}) = -|A_{xy}|\hat{p}_x + |A_z|\hat{p}_z$, namely this is the polar state. At $\theta = 0$, the OP is now $\Delta(\hat{\mathbf{p}}) = -i|A_{xy}|\hat{p}_y + |A_z|\hat{p}_z$. This is a superposition of the polar state and the chiral state. The spatial position where the arrow of l -vector near the HQV core vanishes is the polar state, and on the opposite side of HQV core, the chiral state is superposed by the polar state. Since this HQV breaks the reflection symmetry, the isolated HQV is energetically disfavored and rather a pair of the HQV is advantageous. This is one of the reasons why we found a pair of the HQV at $\Omega = 0.4\omega_{\perp}$.

Upon further increase in the rotational speed ($\Omega = 0.5\omega_{\perp}$), the HQVs enter further from the x direction (see Fig. 4). They are different from above mentioned plus HQVs. As is seen from Fig. 5(b), a pair of plus-minus HQVs appears from the x direction. There are the vortices with the winding number 1 in each A_+ and A_- component on the different position of the x axis. The depletion of the OP amplitude by the vortices is compensated by the growth of amplitude with the opposite orbital angular momentum component. The minus HQV is situated more inside in the trap potential than plus HQV, because of the repulsive interaction between the plus HQV on the x axis and the y axis. It is an analogous situation for the HQVs in the $F = 1$ spinor BEC.³¹⁾ We also notice from Fig. 4 ($\Omega = 0.5\omega_{\perp}$) that the condensate profile itself expands, deforms and deviates clearly from a circular form due to the non-trivial centrifugal energy.

Figure 6 shows a different view of Fig. 4, displaying the z - x cross section. At rest, the l -vectors point almost to the x direction. As Ω increases, the downward l_z component appears, which causes a counterclockwise circular ‘‘orbital’’ supercurrent. At the top and bottom ends of the system the HQVs appear as indicated by asterisks. These blue lines show the polar state neighboring the HQV as mentioned above. In the $\Omega = 0.5\omega_{\perp}$ case, the side view of two pairs of plus-minus HQVs can be seen clearly. The light blue lines indicated by the red arrows correspond to the polar states between plus and minus HQV. These lines bend outward away from the center towards $\pm z$ direction. Around the positions indicated by the red arrows the condensate profile is greatly deformed. Because there the polar state dominates over the chiral state, which leads to the depletion of the condensate, resulting in this deformation.

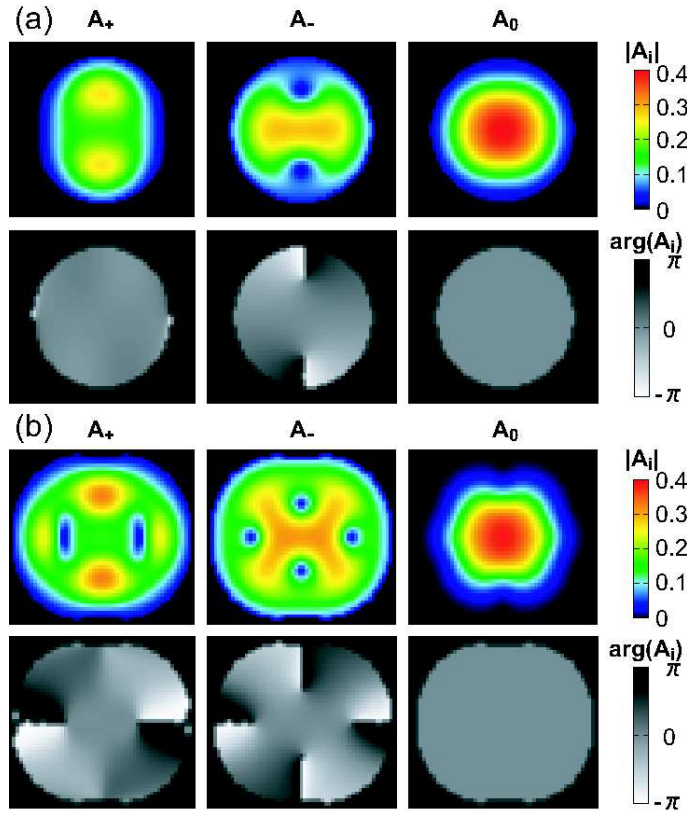


Fig. 5. (Color online) The amplitude (upper) and phase (lower) of the OP components A_+ , A_- and A_0 in the x - y plane at $z = 0$ corresponding to Fig. 4. (a) At $\Omega = 0.4\omega_\perp$ the vortices with winding number 1 enter A_- component. The depletion of the OP amplitude by the vortices is compensated by the growth of A_+ amplitude. (b) At $\Omega = 0.5\omega_\perp$ the vortices with winding number 1 appear. The vortices on the y and x axis are plus and plus-minus HQVs, respectively.

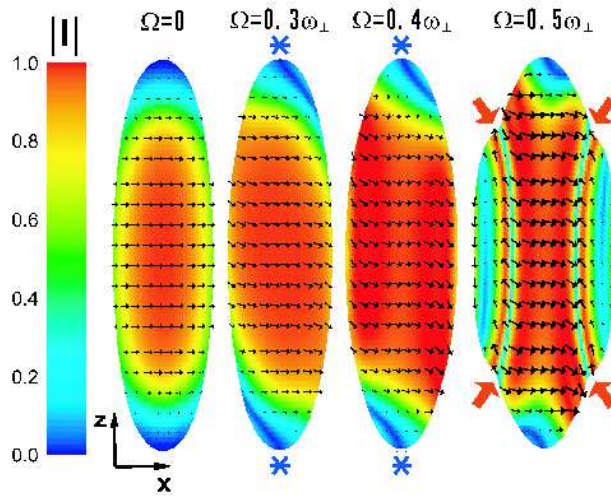


Fig. 6. (Color online) The z - x cross sections corresponding to Fig. 4. The l -vectors lie almost in the x - y plane at rest. Under rotation two HQVs appear, shown as asterisks. At $\Omega = 0.5\omega_\perp$ two pairs of the HQVs can be seen, indicated by red arrows.

5. Pancake Shape Trap

In order to understand the geometric effect of the textures stabilized in cigar shape trap, we examine the pancake trap case. We consider the anisotropy $\lambda = 3.0$ as an example, where we take $100 \times 100 \times 80$ meshes with the cloud size $R_x = R_y = 30$ and $R_z = 10$ in the Thomas-Fermi approximation. We fix the temperature at $t_x = t_y = 0.5$ and $\alpha = 0.95$.

5.1 Axis symmetric texture at rest

Figure 7 displays the resulting l -vector texture (Fig. 7(a)) and associated in-plane supercurrent (Fig. 7(b)) at rest. It is seen that most of the l -vectors point to the negative z direction, except for those near the upper and lower surface regions, which acquire the r -component of the radial direction. The trap potential forces the l -vector to be parallel to the surface of condensates. This effect is especially strong when the curvature of the surface is large. Thus, in this case shown in Fig. 7(a), the left and right ends of the system force the l -vectors to point to the z direction, giving an overall l -vector configuration to the z direction, even for the vectors near the center. The amplitude of the l -vectors decrease, namely the polar state mixes with the chiral state towards the outside.

This stable texture is axis symmetric around the z axis, which is different in the cigar shape trap. This is because the effect of the trap potential is greater than one of the dipole-dipole interaction in the present situation ($\alpha = 0.95$), so that the chiral state consisting of the \hat{p}_x and \hat{p}_y components dominates over the polar state, resulting in the axis symmetric texture with respect to the z axis. If the influence of the dipole-dipole interaction is much greater, or α becomes small, the stable texture is similar to those in the cigar shape trap.

The spatial variation of the amplitude of l -vectors towards the outer region generates a circular “orbital” supercurrent in the x - y plane as shown in Fig. 7(b). Since the spontaneous supercurrent flows around the external rotational axis, the axial symmetric texture is stable against low rotation.

5.2 Vortices under rotation

As shown in Fig. 8 where the x - y cross section at $z = 0$ is displayed for various rotations. Similarly to the previous texture changes in the cigar shape, we see a pair of the HQV enter from the y axis for $\Omega = 0.3\omega_\perp$. Those vortices are exactly the same HQV as in the cigar case (see Fig. 4). The following sequence upon increasing Ω is very similar to the previous cigar case, slightly differing its rotation speed where in the pancake case the sequence is shifted to lower speed. We illustrate the x - z cross section at $y = 0$ in Fig. 9. The almost l -vectors pointing to the negative z direction at rest now deforms as Ω increases. From the right and left ends the polar state seen as blue color invades into the system. At $\Omega = 0.5\omega_\perp$ the condensate profile itself is deformed greatly because of the dominance of the polar state associated with increasing HQVs.

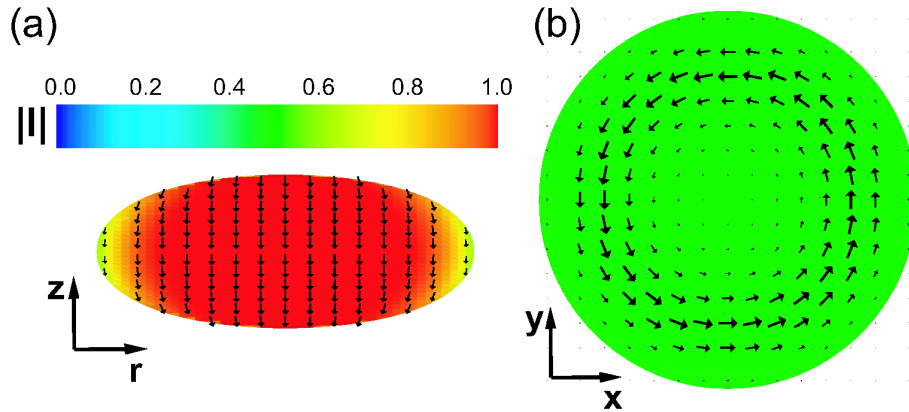


Fig. 7. (Color online) Stable texture in the pancake trap with $\lambda = 3.0$ at rest. (a) l -vector pattern in the z - r plane. The pattern is axial symmetric around z . (b) Spontaneous supercurrent in the x - y plane at $z = 0$.

6. Summary and Discussions

By minimizing the generic GL energy functional within weak coupling approximation, we find stable textures for p -wave superfluids in neutral atomic gases confined in 3D harmonic trap potentials which are to be realized in near future. In order to help detecting its superfluidity, we examine two typical trap geometries, cigar and pancake shapes. At rest, the obtained stable textures in both shapes exhibit the spontaneous supercurrent flow. Under rotation, a pair of the HQVs enters in the condensates. The isolated HQV is never stabilized in our calculations because of topological constrains.

It is interesting to note that the direction of the spontaneously generated supercurrent at rest is always perpendicular to the direction of the majority l -vectors, that is, the condensates in the cigar and pancake case the l -vectors lie on the x - y plane and point to the z direction, respectively, so the supercurrent flows toward the z direction and in the x - y plane. This implies that the trap shape is critical in understanding and controlling the physics of the textures on the p -wave superfluid.

The p -wave Feshbach resonance occurs by using either the same species^{23,24)} or two species with different hyperfine states²⁵⁻²⁷⁾ whose difference in our context amounts to giving different values of the parameter α because the dipole-dipole interaction for a Cooper pair, yielding the splitting between $m_l = \pm 1$ and $m_l = 0$, works differently for two cases.

As for Majorana particle generated in the vortex core in half-quantum vortex, let us examine whether or not the present HQV accommodates the Majorana particle in its core. The Majorana condition is obviously fulfilled when the half-quantum vortex is involved the d -vector, namely the spin degrees of freedom.¹⁶⁾ However, in the present spinless HQV it turns out by examining the Bogoliubov-de Gennes equation³²⁾ that the particles bound in the HQV

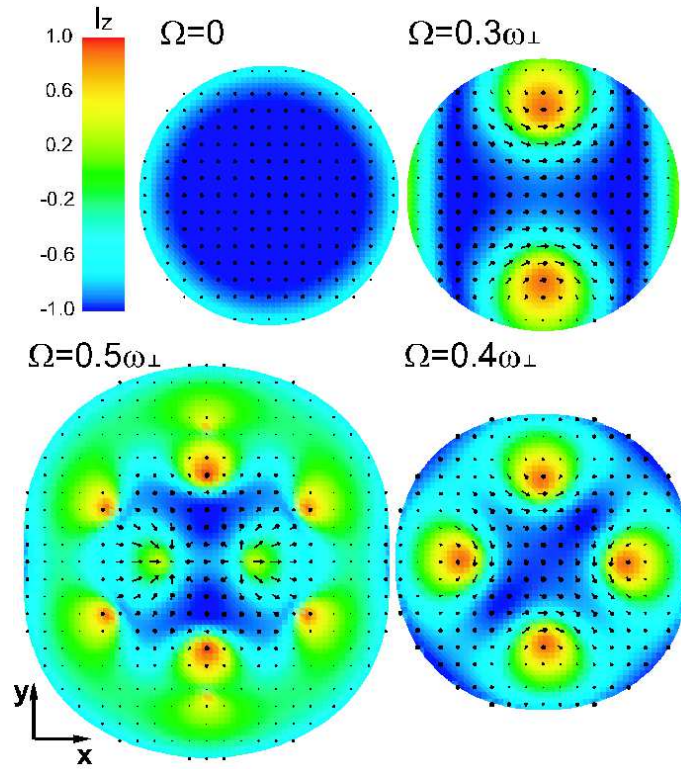


Fig. 8. (Color online) The x - y cross sectional view of the textures for the pancake shape trap with $\lambda = 3.0$ for various rotations. The two objects on the y axis for $\Omega = 0.3\omega_{\perp}$ are the HQVs. Compare those with Fig. 4 in cigar shape case.

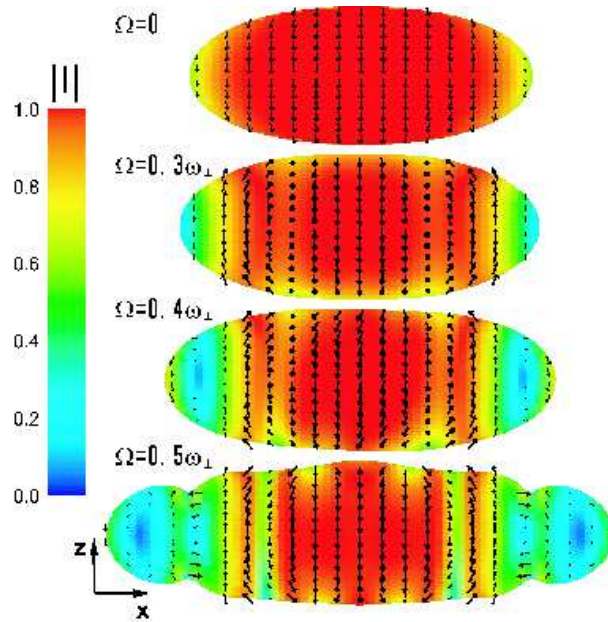


Fig. 9. (Color online) The x - z cross sectional view of the same textures in Fig. 8. The polar state indicated by blue color gradually enter from the right and left ends, making the system deform.

core always have a finite energy, not at zero-energy, which is indispensable for the Majorana condition. Therefore, those are never the Majorana particles. In order to find the Majorana particles, it is necessary to stabilize the singular vortex with odd winding number in chiral superfluids.³²⁾ In the present case, it might be realized for extremely flat pancake limit where the \hat{p}_z component becomes irrelevant. The detailed energetics between the present HQV and the singular vortex belongs to future study.

ACKNOWLEDGMENTS

We wish to thank T. Ohmi, M. Ichioka, T. Mizushima, and T. Kawakami for useful discussions.

Appendix A

We start with the Hamiltonian in a co-rotating frame:

$$H = H_0 - \boldsymbol{\Omega} \cdot \mathbf{L}, \quad (\text{A}\cdot\text{1})$$

$$H_0 = \sum_i [(p_i^2/2m) + U(\mathbf{r}_i)] + V \quad (\text{A}\cdot\text{2})$$

where H_0 is the Hamiltonian in a non-rotating system, consisting of the kinetic energy term, the harmonic trap potential term U and the interaction energy term V . The angular velocity due to the external rotation is $\boldsymbol{\Omega}$ and the angular momentum is $\mathbf{L} = \sum_i 1/2 (\mathbf{r}_i \times \mathbf{p}_i - \mathbf{p}_i \times \mathbf{r}_i)$.

We can write H in the form

$$H = \sum_i \left[\frac{1}{2m} (\mathbf{p}_i - m\mathbf{v}_{n,i})^2 + U(\mathbf{r}_i) \right] + V - \sum_i \frac{1}{2} m\mathbf{v}_{n,i}^2, \quad (\text{A}\cdot\text{3})$$

where $\mathbf{v}_{n,i} = \boldsymbol{\Omega} \times \mathbf{r}_i$ is the ‘‘normal fluid’’ velocity at the location of the particle i . The last term is the centrifugal energy.

The gradient energy given by the first term of the Hamiltonian (A-3)

$$f_{\text{grad}} = \frac{7\zeta(3)N(0)}{16(\pi k_B T_c)^2} [(\mathbf{p}^* - m\mathbf{v}_n)_i A_j^*] [(\mathbf{p} - m\mathbf{v}_n)_k A_l] \langle v_{Fi} \hat{p}_j v_{Fk} \hat{p}_l \rangle_{\hat{\mathbf{p}}}, \quad (\text{A}\cdot\text{4})$$

where $\langle \dots \rangle_{\hat{\mathbf{p}}}$ denotes the Fermi surface average. Taking the contraction of the subscripts in the Fermi surface average, the mean value is finite. Replacing \mathbf{p} with $-i\hbar\nabla$, we obtain the well-known form of the gradient energy⁶⁾

$$f_{\text{grad}} = K_1(\partial_i^* A_j^*)(\partial_i A_j) + K_2(\partial_i^* A_j^*)(\partial_j A_i) + K_3(\partial_i^* A_i^*)(\partial_j A_j). \quad (\text{A}\cdot\text{5})$$

In a similar manner, the centrifugal energy given by the last term of the Hamiltonian (A-3) can be recast into

$$\begin{aligned} f_{\text{cent}} &= -\frac{7\zeta(3)N(0)}{16(\pi k_B T_c)^2} [(m\mathbf{v}_n)_i A_j^*] [(m\mathbf{v}_n)_k A_l] \langle v_{Fi} \hat{p}_j v_{Fk} \hat{p}_l \rangle_{\hat{\mathbf{p}}} \\ &= -\frac{m^2}{\hbar^2} [K_1(\boldsymbol{\Omega} \times \mathbf{r})_i A_j^*(\boldsymbol{\Omega} \times \mathbf{r})_i A_j + K_2(\boldsymbol{\Omega} \times \mathbf{r})_i A_j^*(\boldsymbol{\Omega} \times \mathbf{r})_j A_i] \end{aligned} \quad (\text{A}\cdot\text{6})$$

$$+ K_3(\mathbf{\Omega} \times \mathbf{r})_i A_i^* (\mathbf{\Omega} \times \mathbf{r})_j A_j]. \quad (\text{A}\cdot 7)$$

Taking $\mathbf{\Omega} \parallel \hat{\mathbf{z}}$, and $\mathbf{\Omega} \times \mathbf{r} = \Omega \rho \hat{\boldsymbol{\theta}}$, we finally obtain the expression of the centrifugal potential as

$$f_{\text{cent}} = -\frac{m^2}{\hbar^2} \Omega^2 \rho^2 (K_1 A_i^* A_i + K_2 |A_\theta|^2 + K_3 |A_\theta|^2). \quad (\text{A}\cdot 8)$$

Appendix B

The bulk free energy (5) is written as

$$\begin{aligned} f_{\text{bulk}} = & -(1 - t_x)(|A_x|^2 + |A_y|^2) - (1 - \alpha t_x)|A_z|^2 \\ & + (|A_x|^2 + |A_y|^2 + |A_z|^2)^2 + \frac{1}{2}(A_x^{*2} + A_y^{*2} + A_z^{*2})(A_x^2 + A_y^2 + A_z^2). \end{aligned} \quad (\text{B}\cdot 1)$$

By taking A_x real, $A_y = |A_y|e^{i\theta_y}$ and $A_z = |A_z|e^{i\theta_z}$ without loss of generality, we write it as

$$\begin{aligned} f_{\text{bulk}} = & -(1 - t_x)(|A_x|^2 + |A_y|^2) - (1 - \alpha t_x)|A_z|^2 \\ & + \frac{3}{2}(|A_x|^4 + |A_y|^4 + |A_z|^4) + 2(|A_x|^2|A_y|^2 + |A_y|^2|A_z|^2 + |A_z|^2|A_x|^2) \\ & + |A_x|^2|A_y|^2 \cos 2\theta_y + |A_y|^2|A_z|^2 \cos(2\theta_y - 2\theta_z) + |A_z|^2|A_x|^2 \cos 2\theta_z. \end{aligned} \quad (\text{B}\cdot 2)$$

There are six cases, which are possibly the minimum solutions: (i) $\theta_y = \theta_z = 0$, (ii) $\theta_y = 0$, $\theta_z = \pi/2$, (iii) $\theta_y = \pi/2$, $\theta_z = 0$, (iv) $\theta_y = \pi/2$, $\theta_z = \pi/2$. (v) $\theta_y = \pi/3$, $\theta_z = 2\pi/3$ and (vi) $|A_x|^2 = |A_y|^2 = 0$.

The relevant minimum solutions are found for (ii) and (vi). In the former case (ii) the solution is given by

$$\begin{aligned} f_{\text{bulk}} = & -\frac{1}{16}[3(1 - t_x)^2 - 2(1 - t_x)(1 - \alpha t_x) + 3(1 - \alpha t_x)^2] \\ |A_x|^2 + |A_y|^2 = & \frac{1}{8}[3(1 - t_x) - (1 - \alpha t_x)] \\ |A_z|^2 = & \frac{1}{8}[-(1 - t_x) + 3(1 - \alpha t_x)] \end{aligned} \quad (\text{B}\cdot 3)$$

This solution is valid for $2 + (-3 + \alpha)t_x \geq 0$, which determines the boundary between this phase called the A phase and the single component phase called B phase below. The other solution for (vi) is expressed as

$$\begin{aligned} f_{\text{bulk}} = & -\frac{1}{16}(1 - \alpha t_x)^2 \\ |A_z|^2 = & \frac{1}{3}(1 - \alpha t_x) \end{aligned} \quad (\text{B}\cdot 4)$$

This B phase is described by a single component, thus it corresponds to the so-called polar phase.

References

- 1) D.M. Stamper-Kurn, M.R. Andrews, A.P. Chikkatur, S. Inouye, H.J. Miesner, J. Stenger, and W. Ketterle: Phys. Rev. Lett. **80** (1998) 2027.
- 2) J. Stenger, S. Inouye, D.M. Stamper-Kurn, H.J. Miesner, A.P. Chikkatur, and W. Ketterle: Nature **396** (1998) 345.
- 3) K. Machida and T. Ohmi: J. Phys. Soc. Jpn. **67** (1998) 1122.
- 4) T.-L. Ho: Phys. Rev. Lett. **81** (1998) 742.
- 5) A.J. Leggett: Rev. Mod. Phys. **47** (1975) 331.
- 6) D. Vollhardt and P. Wölfle: *The Superfluid phase of Helium 3* (Taylor and Francis, London, 1990).
- 7) G.E. Volovik: *Exotic Properties of Superfluid ^3He* (World Scientific, Singapore, 1992).
- 8) A.L. Fetter: in *Progress in Low Temperature Physics*, ed D.F. Brewer (Elsevier Science Publishers, Amsterdam, 1986) Vol. X, p. 1.
- 9) M.M. Salomaa and G.E. Volovik: Rev. Mod. Phys. **59** (1987) 533.
- 10) K. Machida, M. Ozaki, and T. Ohmi: J. Phys. Soc. Jpn. **58** (1989) 4116; K. Machida, T. Nishira, and T. Ohmi: J. Phys. Soc. Jpn. **68** (1999) 3364; K. Machida and M. Ozaki: Phys. Rev. Lett. **66** (1991) 3293.
- 11) J.A. Sauls: Adv. Phys. **43** (1994) 113.
- 12) M. Buballa: Phys. Rep. **407** (2005) 205.
- 13) M.G. Alford, A. Schmitt, K. Rajagopal, and T. Schäfer: Rev. Mod. Phys. **80** (2008) 1455.
- 14) See for example, C. Nayak, S.H. Simon, A. Stern, M. Freedman, and S. Das Sarma: Rev. Mod. Phys. **80** (2008) 1083.
- 15) Y. Tsutsumi, T. Kawakami, T. Mizushima, M. Ichioka, and K. Machida: Phys. Rev. Lett. **101** (2008)135302.
- 16) T. Kawakami, Y. Tsutsumi, and K. Machida: Phys. Rev. B **79** (2009) 092506.
- 17) J. Zheng, E.G.M. van Kempen, T. Bourdel, L. Khaykovich, J. Cubizolles, F. Chevy, M. Teichmann, L. Tarruell, S.J.J.M. F. Kokkelmans, and C. Salomon: Phys. Rev. A **70** (2004) 030702(R).
- 18) C.H. Schunck, M.W. Zwierlein, C.A. Stan, S.M.F. Raupach, W. Ketterle, A. Simoni, E. Tiesinga, C.J. Williams, and P.S. Julienne: Phys. Rev. A **71** (2005) 045601.
- 19) Y. Inada, M. Horikoshi, S. Nakajima, M. Kuwata-Gonogami, M. Ueda, and T. Mukaiyama: Phys. Rev. Lett. **101** (2008) 100401.
- 20) C.A. Regal, C. Ticknor, J.L. Bohn, and D.S. Jin: Nature **424**(2003) 47.
- 21) C. Ticknor, C.A. Regal, D.S. Jin, and J.L. Bohn: Phys. Rev. A **69** (2004) 042712.
- 22) J.P. Gaebler, J.T. Stewart, J.L. Bohn, and D.S. Jin: Phys. Rev. Lett. **98** (2007) 200403.
- 23) C.-H. Cheng and S.-K. Yip: Phys. Rev. Lett. **95** (2005) 070404.
- 24) V. Gurarie, L. Radzihovsky, and A.V. Andreev: Phys. Rev. Lett. **94** (2005) 230403.
- 25) T.-L. Ho and R.B. Diener: Phys. Rev. Lett. **94** (2005) 090402.
- 26) K. Quader, R. Liao, and F. Popescu: Int. J. Mod. Phys. B **22** (2008) 4358.
- 27) Y. Ohashi: Phys. Rev. Lett. **94** (2005) 050403.
- 28) Y. Tsutsumi and K. Machida: to be published in Phys. Rev. A.
- 29) M.A. Baranov and D.S. Petrov: Phys. Rev. A **58** (1998) 801(R).
- 30) T. Mizushima, N. Kobayashi, and K. Machida: Phys. Rev. A **70** (2004) 043613; W.V. Pogosov, R. Kawate, T. Mizushima, and K. Machida: Phys. Rev. A **72** (2005) 063605.

- 31) A.-C. Ji, W.M. Liu, J.L. Song, and F. Zhou: Phys. Rev. Lett. **101** (2008) 010402.
- 32) T. Mizushima, M. Ichioka, and K. Machida: Phys. Rev. Lett. **101** (2008) 150409.